

# Simulations of dynamo action in slowly rotating M dwarfs: Dependence on dimensionless parameters

C. A. Ortiz-Rodríguez<sup>1</sup>, P. J. Käpylä<sup>2,3,4</sup>, F. H. Navarrete<sup>5,4</sup>, D. R. G. Schleicher<sup>1</sup>, R. E. Mennickent<sup>1</sup>, J.P. Hidalgo<sup>1</sup>,  
and B. Toro<sup>1</sup>

<sup>1</sup> Departamento de Astronomía, Facultad de Ciencias Físicas y Matemáticas, Universidad de Concepción, Av. Esteban Iturra s/n Barrio Universitario, Casilla 160-C, Chile

<sup>2</sup> Leibniz-Institut für Sonnenphysik (KIS), Schöneckstr. 6, 79104 Freiburg, Germany

<sup>3</sup> Institut für Astrophysik und Geophysik, Georg-August-Universität Göttingen, Friedrich-Hund-Platz 1, 37077 Göttingen, Germany

<sup>4</sup> Nordita, KTH Royal Institute of Technology and Stockholm University, 10691 Stockholm, Sweden

<sup>5</sup> Hamburger Sternwarte, Universität Hamburg, Gojenbergsweg 112, 21029 Hamburg, Germany

## ABSTRACT

**Aims.** The aim of this study is to explore the magnetic and flow properties of fully convective M dwarfs as a function of rotation period  $P_{\text{rot}}$  and magnetic Reynolds  $\text{Re}_M$  and Prandtl numbers  $\text{Pr}_M$ .

**Methods.** We performed three-dimensional simulations of fully convective stars using a star-in-a-box setup. This setup allows global dynamo simulations in a sphere embedded in a Cartesian cube. The equations of non-ideal magnetohydrodynamics were solved with the PENCIL CODE. We used the stellar parameters of an M5 dwarf with  $0.21M_{\odot}$  at three rotation rates corresponding to rotation periods ( $P_{\text{rot}}$ ): 43, 61 and 90 days, and varied the magnetic Prandtl number in the range from 0.1 to 10.

**Results.** We found systematic differences in the behaviour of the large-scale magnetic field as functions of rotation and  $\text{Pr}_M$ . For the simulations with  $P_{\text{rot}} = 43$  days and  $\text{Pr}_M \leq 2$ , we found cyclic large-scale magnetic fields. For  $\text{Pr}_M > 2$  the cycles vanish and field shows irregular reversals. In simulations with  $P_{\text{rot}} = 61$  days for  $\text{Pr}_M \leq 2$  the cycles are less clear and the reversals are less periodic. In the higher- $\text{Pr}_M$  cases, the axisymmetric mean field shows irregular variations. For the slowest rotation case with  $P_{\text{rot}} = 90$  days, the field has an important dipolar component for  $\text{Pr}_M \leq 5$ . For the highest  $\text{Pr}_M$  the large-scale magnetic field is predominantly irregular at mid-latitudes, with quasi-stationary fields near the poles. For the simulations with cycles, the cycle period length slightly increases with increasing  $\text{Re}_M$ .

**Key words.** convection, dynamo, stars: magnetic field, stars: low-mass, magnetohydrodynamics (MHD)

## 1. Introduction

Magnetic fields in stars have been studied both theoretically and through observations, particularly magnetic fields of solar-type main-sequence stars (e.g. Brun & Browning 2017, and references therein). M dwarfs are low-mass main-sequence stars with a structure that undergoes a transition from fully convective for masses up to  $0.35M_{\odot}$  to a solar-like structure (radiative core and convective envelope) for higher mass (Chabrier & Baraffe 1997). These stars are found to be magnetically active, as shown by Saar & Linsky (1985) where surface magnetic activity was confirmed for M dwarfs with infrared measurements. Today there is considerable observational evidence of magnetic activity in M dwarfs that show magnetic field strengths reaching up to a few kG (see Kochukhov 2021, and references therein). Because of the lack of a tachocline, the shear layer between the radiative and convective zones, fully convective M dwarfs are quite interesting from the point of view of dynamo theory and can help us to understand whether a tachocline has a strong impact on the dynamo itself. In this context, Wright & Drake (2016) reported that the X-ray emission of fully and partially convective stars follows a similar trend with the Rossby number  $\text{Ro} = P_{\text{rot}}/\tau$ , which is the ratio of the rotation period and convective turnover time, and which measures the rotational influence on convective flows. It was found that the X-ray emission increases with decreasing  $\text{Ro}$  until  $\text{Ro} \approx 0.1$ , and for smaller  $\text{Ro}$  the X-ray lu-

minosity saturates. Furthermore, Newton et al. (2017) found a similar trend, a saturated relation between the chromospheric  $\text{H}\alpha$  emission and  $\text{Ro}$  for rapidly rotating M dwarfs and a power-law decay of the  $\text{H}\alpha$  emission with increasing  $\text{Ro}$  for slowly rotating stars. The transition occurs near  $\text{Ro} = 0.2$ . In addition, Doppler and Zeeman-Doppler inversions have revealed that fully convective M dwarfs often show large-scale magnetic fields and that for rapid enough rotation both dipolar and multipolar fields are possible (e.g. Morin et al. 2010; Kochukhov 2021). Furthermore, Klein et al. (2021) found that the fully convective star Proxima Centauri has a seven year activity cycle.

Numerical simulations of stars are performed to achieve a better understanding of their magnetic fields, dynamos, and convection as functions of stellar parameters and dimensionless quantities, such as the magnetic Prandtl number, which is an intrinsic property of the fluid defined by the ratio of kinematic viscosity  $\nu$  and resistivity  $\eta$  of the plasma. Some authors have performed magnetohydrodynamic (MHD) simulations of fully convective M dwarfs, which are particularly interesting for comparison with solar dynamo models due to the lack of a tachocline. The first simulations of fully convective M dwarfs were presented by Dobler et al. (2006), who used a star-in-a-box model to study dynamos as a function of rotation. They found predominantly quasi-static large-scale magnetic fields and typically weak or anti-solar differential rotation with faster poles and slower equator. These simulations had relatively modest fluid

and magnetic Reynolds numbers as well as low density stratification. [Browning \(2008\)](#) presented simulations of fully convective M dwarfs using the anelastic magnetohydrodynamic equations, considering a spherical domain extending from 0.08 to 0.96 stellar radius, finding magnetic fields with significant axisymmetric components. In simulations without magnetic fields, the differential rotation is strong and solar-like with fast equator and slow poles, while in magnetic simulations it is reduced, and tends to a solid body rotation in the most turbulent magnetohydrodynamical simulations. A similar numerical approach was taken in the studies of [Yadav et al. \(2015\)](#) and [Yadav et al. \(2016\)](#) who used strongly stratified anelastic simulations to study the coexistence of dipolar and multipolar dynamos and cyclic solutions at relatively slow rotation corresponding to parameter regime similar to Proxima Centauri, respectively. More recently, [Brown et al. \(2020\)](#) performed simulations of fully convective M dwarfs in spherical coordinates, finding cyclic hemispheric dynamos in their models.

The rotation period of the star,  $P_{\text{rot}}$ , is a key factor that determines the nature of the dynamo. This is evidenced by observational studies of M dwarfs, which demonstrate that with decreasing  $P_{\text{rot}}$  the magnetic field strength increases (e.g. [Wright et al. 2018](#); [Reiners et al. 2022](#)). This has also been shown numerically by, for example, [Käpylä \(2021\)](#) who used a star-in-a-box model for fully convective stars and found increasing magnetic field strength with decreasing rotation period. Furthermore, different dynamo modes were found as a function of rotation in that work. Slowly rotating stars have mostly axisymmetric and quasi-steady large-scale magnetic fields, for intermediate rotation the large-scale field is mostly axisymmetric and cyclic, and in the case of rapid rotation, the large-scale magnetic fields are predominantly non-axisymmetric with a dominant  $m = 1$  mode. As demonstrated by [Käpylä \(2021\)](#), the large-scale dynamo is sustained even in the absence of a tachocline. In this sense, the work by [Bice & Toomre \(2020\)](#) using simulations of early M dwarfs supports the hypothesis that the tachocline is not necessary for producing strong toroidal magnetic fields, although it may generate stronger fields in faster rotators.

In this paper, we present three-dimensional MHD simulations of fully convective M dwarfs with the star-in-a-box setup described in [Käpylä \(2021\)](#) (see also [Dobler et al. 2006](#)). Our main goal is to explore the dependence on dimensionless parameters, in particular the magnetic Prandtl and Reynolds numbers  $\text{Pr}_M$  and  $\text{Re}_M$ , which are crucial ingredients for dynamos and plasmas in general. High and low values of  $\text{Pr}_M$  and  $\text{Re}_M$  lead to very different dynamo scenarios; at low  $\text{Pr}_M$  the magnetic energy is dissipated in the inertial range of the flow and small-scale dynamo action requires a much higher  $\text{Re}_M$  to be excited (e.g. [Schekochihin et al. 2007](#); [Käpylä et al. 2018](#)). On the other hand, stars typically have  $\text{Pr}_M \ll 1$  and  $\text{Re}_M \gg 1$  (e.g. [Augustson et al. 2019](#); [Jermyn et al. 2022](#)). Our simulations were performed for a set of rotation periods  $P_{\text{rot}}$  ranging from 43 to 90 days, the latter being the rotation period of Proxima Centauri, and for values of  $\text{Pr}_M$  and  $\text{Re}_M$  ranging from 0.1 to 10 and 21 to over 1400, respectively, which is the numerically feasible range for this type of simulations. The methods and model are described in Section 2, while the description and analysis of the results is provided in Section 3. We discuss the conclusions in Section 4.

## 2. Methods

### 2.1. The model

We use the star-in-a-box model described in [Käpylä \(2021\)](#), which is based on the set-up of [Dobler et al. \(2006\)](#). The model allows dynamo simulations of entire stars. In the present scenario, we use a sphere of radius  $R$  that is enclosed in a cube with side  $2.2R$ . We solve the induction, continuity, momentum, and energy conservation equations:

$$\frac{\partial \mathbf{A}}{\partial t} = \mathbf{u} \times \mathbf{B} - \eta \mu_0 \mathbf{J}, \quad (1)$$

$$\frac{D \ln \rho}{Dt} = -\nabla \cdot \mathbf{u}, \quad (2)$$

$$\frac{D \mathbf{u}}{Dt} = -\nabla \Phi - \frac{1}{\rho} (\nabla p - \nabla \cdot 2\nu \rho \mathbf{S} + \mathbf{J} \times \mathbf{B}) - 2\boldsymbol{\Omega} \times \mathbf{u} + \mathbf{f}_d, \quad (3)$$

$$T \frac{Ds}{Dt} = \frac{1}{\rho} [\mathcal{H} - C - \nabla \cdot (\mathbf{F}_{\text{rad}} + \mathbf{F}_{\text{SGS}})] + 2\nu \mathbf{S}^2 + \frac{\mu_0 \eta \mathbf{J}^2}{\rho}, \quad (4)$$

where  $\mathbf{A}$  is the magnetic vector potential,  $\mathbf{u}$  is the velocity field,  $\mathbf{B} = \nabla \times \mathbf{A}$  is the magnetic field,  $\mu_0$  is the magnetic permeability of vacuum,  $\eta$  is the magnetic diffusivity,  $\rho$  is the density of the fluid,  $D/Dt = \partial/\partial t + \mathbf{u} \cdot \nabla$  is the advective derivative,  $T$  is the temperature,  $\Phi$  is the gravitational potential,  $p$  is the pressure,  $\nu$  is the kinematic viscosity,  $s$  is the specific entropy,  $\mathbf{J} = \nabla \times \mathbf{B}/\mu_0$  is the current density,  $\boldsymbol{\Omega} = \Omega_0 \hat{\mathbf{z}}$  is the rotation vector, with  $\Omega_0$  being the mean angular velocity of the star and  $\hat{\mathbf{z}}$  the unit vector along the rotation axis, and  $\mathbf{S}$  is the traceless rate-of-strain tensor,

$$S_{ij} = \frac{1}{2}(u_{i,j} + u_{j,i}) - \frac{1}{3}\delta_{ij}\nabla \cdot \mathbf{u}, \quad (5)$$

where the commas denote differentiation.  $\mathcal{H}$  and  $C$  describe heating and cooling, and  $\mathbf{f}_d$  describes the damping of flows outside the star (see [Käpylä 2021](#), for more details). The radiative flux is given by

$$\mathbf{F}_{\text{rad}} = -K\nabla T, \quad (6)$$

where  $K$  corresponds to Kramers opacity law, where its power-law exponents are the same of [Käpylä \(2021\)](#). The subgrid-scale (SGS) entropy flux  $\mathbf{F}_{\text{SGS}}$  damps fluctuations near the grid scale, but contributes only negligibly to the net energy transport. It is given by

$$\mathbf{F}_{\text{SGS}} = -\chi_{\text{SGS}}\rho\nabla s', \quad (7)$$

where  $\chi_{\text{SGS}}$  is the SGS diffusion coefficient,  $s' = s - \bar{s}_t$  is the entropy fluctuation and  $\bar{s}_t$  is a running temporal mean of the entropy. Note that the SGS flux used here does not include the temperature  $T$ . This form of the SGS flux is appropriate if the entropy equation is solved, whereas the  $T$  factor appears in the SGS term if the corresponding energy equation was solved ([Rogachevskii & Kleorin 2015](#)).

The simulations were run with the PENCIL CODE<sup>1</sup> ([Pencil Code Collaboration et al. 2021](#)), which is a high-order finite-difference code for solving partial differential equations with primary applications in compressible astrophysical magnetohydrodynamics (MHD).

#### 2.1.1. Dimensionless parameters

Each simulation is characterized by various dimensionless numbers. These parameters are usually order of magnitude ratios of

<sup>1</sup> <https://github.com/pencil-code>

various terms in the MHD equations or of the corresponding timescales.

The effect of rotation relative to viscosity is measured by the Taylor number, given by

$$\text{Ta} = \frac{4\Omega_0^2 R^4}{\nu^2}. \quad (8)$$

The Coriolis number is a measure of the influence of rotation on the flow

$$\text{Co} = \frac{2\Omega_0}{u_{\text{rms}} k_R}, \quad (9)$$

where  $u_{\text{rms}}$  is the volume-averaged root-mean-square velocity and  $k_R = 2\pi/R$  is the scale of the largest convective eddies. Another definition of the Coriolis number used in other studies (e.g. Brown et al. 2020; Käpylä 2021) is based on the vorticity, and considers the local lengthscale. This is defined by

$$\text{Co}_\omega = \frac{2\Omega_0}{\omega_{\text{rms}}}, \quad (10)$$

where  $\omega_{\text{rms}}$  is the volume averaged rms vorticity, with  $\omega = \nabla \times \mathbf{u}$ . The fluid and magnetic Reynolds numbers, SGS and magnetic Prandtl, and SGS Péclet numbers are defined as

$$\text{Re} = \frac{u_{\text{rms}}}{\nu k_R}, \quad \text{Re}_M = \frac{u_{\text{rms}}}{\eta k_R}, \quad (11)$$

$$\text{Pr}_{\text{SGS}} = \frac{\nu}{\chi_{\text{SGS}}}, \quad \text{Pr}_M = \frac{\nu}{\eta}, \quad \text{Pe} = \frac{u_{\text{rms}}}{\chi_{\text{SGS}} k_R}. \quad (12)$$

### 2.1.2. Physical units and nondimensional quantities

We model a main-sequence (M5) dwarf with the same stellar parameters as in Dobler et al. (2006) and Käpylä (2021). The mass, radius, and luminosity of the star are  $M_\star = 0.21M_\odot$ ,  $R_\star = 0.27R_\odot$ , and  $L_\star = 0.008L_\odot$ , respectively. We use an enhanced luminosity approach (Käpylä et al. 2020) to reduce the gap between the thermal and dynamical timescales, such that fully compressible simulations are feasible. This implies that the results need to be scaled suitably for comparison with real stars. The conversion factor between the rotation rate, length, time, velocity, and magnetic fields in the simulation and in physical units are the same as those used by Käpylä (2021) (see their Appendix A). Nondimensional quantities are obtained by using the stellar radius as the unit of length  $[x] = R$ . Time is given in terms of the free-fall time  $\tau_{\text{ff}} = \sqrt{R^3/GM}$ , the unit of velocity is  $[U] = R/\tau_{\text{ff}}$ , and magnetic fields are given in terms of the equipartition field strength  $B_{\text{eq}} = \langle \sqrt{\mu_0 \rho U^2} \rangle$ , where  $\langle \cdot \rangle$  stands for time and volume averaging.

## 3. Results

We present a set of 3D MHD simulations in the slow to intermediate rotation regime with global Coriolis number  $\text{Co}$  ranging between 3.1 and 12.9 (see Table 1). The rotation rates are  $\bar{\Omega} = 1.0, 0.7$  and  $0.5$  (which correspond to  $P_{\text{rot}} = 43, 61,$  and  $90$  days) in sets A, B, and C, respectively. The magnetic Prandtl number  $\text{Pr}_M$  varies set between 0.1 and 10 (0.5 and 10) in set A (sets B and C).

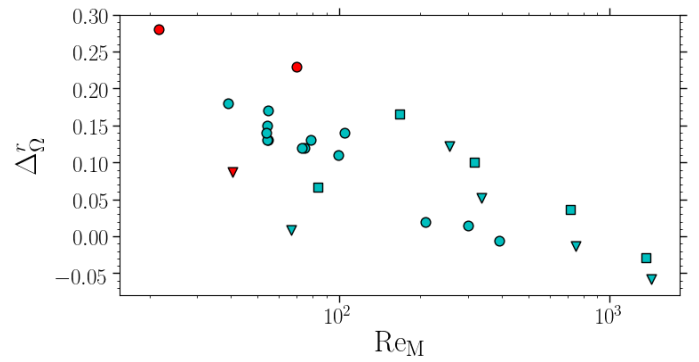


Fig. 1: Amplitude of the radial differential rotation as a function of the magnetic Reynolds number for simulations of set A (circles), B (squares) and C (triangles). Cyan (red) is for simulations with dynamo (without dynamo).

### 3.1. Flow properties

#### 3.1.1. Differential rotation and meridional circulation

The averaged rotation rate in cylindrical coordinates is given by

$$\bar{\Omega}(\varpi, z) = \Omega_0 + \bar{U}_\phi(\varpi, z)/\varpi, \quad (13)$$

where  $\varpi = r \sin \theta$  is the cylindrical radius, and where the overbar denotes azimuthal averaging. The averaged meridional flow is given by

$$\bar{U}_{\text{mer}}(\varpi, z) = (\bar{U}_\varpi, 0, \bar{U}_z). \quad (14)$$

The angular velocity does not only vary with depth but also with latitude. A way to quantify this is by measuring the amplitude of the radial and latitudinal differential rotation with

$$\Delta_\Omega^{(r)} = \frac{\bar{\Omega}_{\text{top,eq}} - \bar{\Omega}_{\text{bot,eq}}}{\bar{\Omega}_{\text{top,eq}}}, \quad (15)$$

$$\Delta_\Omega^{(\bar{\theta})} = \frac{\bar{\Omega}_{\text{top,eq}} - \bar{\Omega}_{\text{top,\bar{\theta}}}}{\bar{\Omega}_{\text{top,eq}}}, \quad (16)$$

where the subscripts top, bot, eq, and  $\bar{\theta}$  correspond to  $R = 0.9R$ ,  $r = 0.1R$ ,  $\theta = 0^\circ$ , and an average of  $\bar{\Omega}$  for latitudes  $+\theta$  and  $-\theta$  in spherical coordinates, respectively.

Values of  $\Delta_\Omega^{(r)}$  and  $\Delta_\Omega^{(\bar{\theta})}$  are listed in Table 2. Positive values of  $\Delta_\Omega^{(r)}$  indicate solar-like differential rotation. We find that  $\Delta_\Omega^{(r)}$  has a tendency to decrease with increasing  $\text{Re}_M$ , which is equivalent to an increasing  $\text{Pr}_M$  (second column of Table 2). Figure 1 shows  $\Delta_\Omega^{(r)}$  as a function of  $\text{Re}_M$  for sets A (circles), B (squares) and C (triangles) confirming the decreasing trend as a function of  $\text{Re}_M$ . The red circles show simulations without dynamos (A8 and A12) and low magnetic Reynolds numbers, where  $\Delta_\Omega^{(r)}$  is higher. Such reduction or quenching of the differential rotation by magnetic fields especially at high  $\text{Re}_M$  has been shown earlier by various simulations, for example, in Brun et al. (2004), Schrunner et al. (2012), and Käpylä et al. (2017). The differential rotation profiles for three representative simulations A1, A16 and A8 are shown in Fig. 2. The rotation profile in run A1 is solar-like; the profile is similar in the rest of simulations with  $\text{Pr}_M \leq 2$ . In run A16 with  $\text{Pr}_M = 10$ , the amplitude of the latitudinal differential rotation is positive whereas the amplitude of the radial differential rotation is negative since the angular velocity does not change considerably with depth at the equator. The middle panel of Fig. 2

Table 1: Simulation parameters.

Sim	$\tilde{\Omega}$	$\tilde{u}_{\text{rms}}$	$B_{\text{rms}} [B_{\text{eq}}]$	$\text{Pr}_{\text{M}}$	$\text{Pr}_{\text{SGS}}$	$\text{Re}_{\text{M}}$	$\text{Re}$	$\text{Co}$	$\text{Co}_{\omega}$	$\text{Ta}$	$\text{Pe}$	Grid
A1	1.0	0.022	0.92	0.1	0.04	55	549	9.2	1.4	$4.00 \cdot 10^{10}$	22	$200^3$
A2	1.0	0.021	0.94	0.1	0.04	79	788	9.3	1.2	$8.30 \cdot 10^{10}$	32	$288^3$
A3	1.0	0.021	0.91	0.2	0.08	54	272	9.3	1.6	$1.00 \cdot 10^{10}$	22	$200^3$
A4	1.0	0.022	0.81	0.5	0.20	54	109	9.3	1.9	$1.60 \cdot 10^9$	22	$200^3$
A5	1.0	0.022	0.75	0.7	0.28	55	78	9.2	2.0	$8.16 \cdot 10^8$	22	$200^3$
A6	1.0	0.020	0.91	0.7	0.28	75	107	9.7	2.0	$1.69 \cdot 10^9$	30	$200^3$
A7	1.0	0.021	0.84	0.9	0.20	54	108	9.4	1.9	$1.60 \cdot 10^9$	22	$200^3$
A8*	1.0	0.030	–	0.2	0.28	22	108	6.6	1.8	$8.16 \cdot 10^8$	30	$200^3$
A9	1.0	0.022	0.71	0.5	0.28	39	78	9.3	2.1	$8.16 \cdot 10^8$	22	$200^3$
A10	1.0	0.020	0.89	1.0	0.20	105	105	9.7	1.9	$1.60 \cdot 10^9$	21	$200^3$
A11	1.0	0.020	0.88	1.0	0.28	73	73	9.9	2.1	$8.16 \cdot 10^8$	20	$200^3$
A12*	1.0	0.028	–	1.0	0.40	70	70	7.2	2.0	$4.00 \cdot 10^8$	28	$200^3$
A13	1.0	0.019	0.81	2.0	0.40	99	50	10.1	2.3	$4.00 \cdot 10^8$	20	$200^3$
A14	1.0	0.017	1.20	5.0	0.40	208	42	12.1	2.4	$4.00 \cdot 10^8$	17	$200^3$
A15	1.0	0.017	1.16	7.0	0.40	300	42	12.0	2.5	$4.00 \cdot 10^8$	17	$200^3$
A16	1.0	0.016	1.24	10.0	0.40	390	39	12.9	2.5	$4.00 \cdot 10^8$	16	$200^3$
B1	0.7	0.024	0.68	0.5	0.40	84	167	5.9	1.1	$1.51 \cdot 10^9$	62	$200^3$
B2	0.7	0.024	0.74	1.0	0.40	168	168	5.8	1.0	$1.51 \cdot 10^9$	68	$576^3$
B3	0.7	0.022	0.88	2	0.40	315	158	6.2	1.0	$1.51 \cdot 10^9$	64	$576^3$
B4	0.7	0.020	1.03	5	0.40	714	143	6.9	1.1	$1.51 \cdot 10^9$	58	$576^3$
B5	0.7	0.019	1.02	10	0.40	1360	135	7.2	1.2	$1.51 \cdot 10^9$	55	$576^3$
C1	0.5	0.025	0.80	1.0	0.20	256	256	3.9	0.6	$1.60 \cdot 10^9$	51	$576^3$
C2*	0.5	0.032	–	0.5	0.40	41	21	3.1	0.9	$1.00 \cdot 10^8$	32	$200^3$
C3	0.5	0.026	0.53	1.0	0.40	67	67	3.8	1.1	$1.00 \cdot 10^8$	27	$200^3$
C4	0.5	0.024	0.85	2	0.40	337	168	4.1	0.7	$7.71 \cdot 10^8$	68	$576^3$
C5	0.5	0.021	1.17	5	0.40	750	150	4.7	0.7	$7.71 \cdot 10^8$	60	$576^3$
C6	0.5	0.020	1.02	10	0.40	1419	142	4.9	0.8	$7.71 \cdot 10^8$	51	$576^3$

**Notes.** Summary of the simulations. From left to right the columns correspond to the simulation name,  $\tilde{\Omega} = \Omega\tau_{\text{ff}}$  is the normalized rotation rate,  $\tilde{u}_{\text{rms}} = u_{\text{rms}}/(GM/R)^{1/2}$  is the normalized root-mean-square velocity,  $B_{\text{rms}}$  is the root-mean-square magnetic field strength in units of the equipartition strength,  $\text{Pr}_{\text{M}}$  and  $\text{Pr}_{\text{SGS}}$  are the magnetic and sub-grid-scale Prandtl numbers,  $\text{Re}_{\text{M}}$  and  $\text{Re}$  are the magnetic and fluid Reynolds numbers,  $\text{Co}$  and  $\text{Co}_{\omega}$  are the global and local Coriolis numbers,  $\text{Ta}$  is the Taylor number and  $\text{Pe}$  is the Péclet number. The last column indicates the grid resolution. Asterisks indicate runs with no dynamo.

shows that the rotation rate at the equator is in fact higher than average almost everywhere and the negative value of  $\Delta_{\Omega}^{(r)}$  is due to the slower than average rotation only very near the surface. Therefore the differential rotation is solar-like. Another method to classify the rotation profile (solar-like or anti-solar) is to use the mean rotation profile at the equator, which, as indicated in Käpylä (2023), can help prevent erroneous conclusions. Furthermore, the profiles in Fig. 2 are symmetric with respect to the equator as in the other simulations performed in this work.

The global Coriolis number (see Eq. 9) in the current simulations ranges from 3.1 to 13. All of our runs show solar-like differential rotation, which is consistent with Käpylä (2021), where the shift from anti-solar to solar-like differential rotation occurs for Coriolis number between 0.7 and 2. This is also consistent with simulations of spherical shell convection by Viviani et al. (2018), which show that the transition occurs around  $\text{Co} = 3$ . (see Table 5 of their work). More recently, Käpylä (2023) found that the transition from anti-solar to solar-like differential rotation depends on the sub-grid scale Prandtl number ( $\text{Pr}_{\text{SGS}}$ ), such that solar-like differential rotation is more difficult to obtain at high  $\text{Pr}_{\text{SGS}}$  than at  $\text{Pr}_{\text{SGS}} \leq 1$ . In this work, all the simulations have  $\text{Pr}_{\text{SGS}} \leq 1$ .

Simulations A8, A12, and C2 do not have dynamos, and they are considered as kinematic cases. The right panel of Fig. 2 displays the rotation profile for simulation A8. It demonstrates that

a faster than average angular velocity spans a broader latitudinal range and a narrower radial range when compared to simulations with dynamo. This depicts the influence of a magnetic field on differential rotation. In the regime  $\text{Pr}_{\text{M}} < 2$  of our simulations, the meridional flow is composed of multiple small cells, while in the regime  $\text{Pr}_{\text{M}} \geq 2$ , the pattern is composed of two to three large cells which are symmetric with respect to the equator. The maximum values of the normalized meridional flow amplitude,  $\tilde{U}_{\text{mer}}^{\text{rms}} = (GM/R)^{-1/2}(\overline{U_{\varphi}^2} + \overline{U_z^2})^{1/2}$ , in the cases shown in Fig. 2 correspond to  $\tilde{U}_{\text{mer}}^{\text{max}} = 0.009, 0.005$  and  $0.023$  for simulations A1, A16 and A8, respectively. The rms value of the meridional velocity is given in the fifth column of Table 2. In the simulations with no dynamo, A8, A12 and C2 (A8 in right panel in Fig. 2), the meridional circulation also exhibits similar multiple patterns, which are also symmetric with respect to the equator.

### 3.1.2. Power spectra and kinetic helicity

To characterize the convective flows we calculated the normalized kinetic energy power spectra (e.g. Viviani et al. 2018; Navarrete et al. 2022) from

$$P_{\text{kin}} = \frac{E_{\text{kin},\ell}}{\sum_{\ell} E_{\text{kin},\ell}}, \quad (17)$$

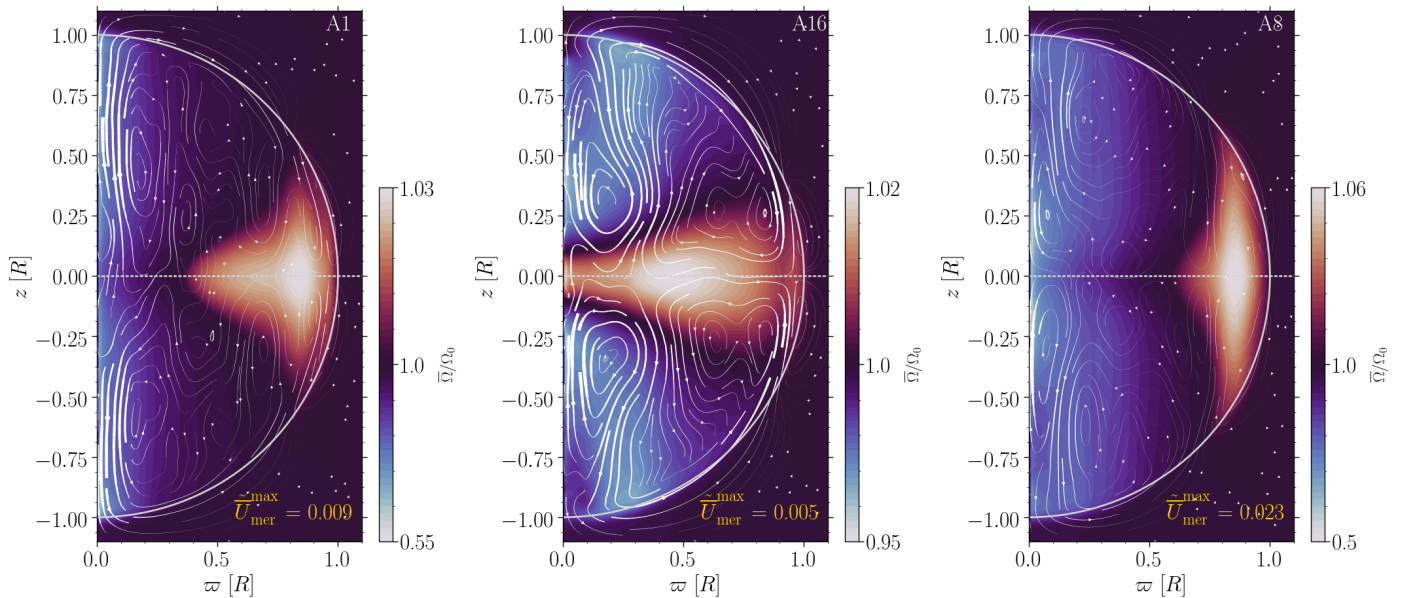


Fig. 2: Normalized time-averaged mean angular velocity  $\bar{\Omega}/\Omega_0$  for simulations A1 (left), A16 (middle), and A8 (right). The colored contours indicate  $\bar{\Omega}(\varpi, z)$ . The streamlines indicate the mass flux due to meridional circulation. The amplitude of the meridional flow speed ( $\bar{U}_{\text{mer}}^{\text{max}}$ ) is indicated in the lower right corner of each panel. The surface is indicated by the gray line while the equator is indicated by the gray dotted line.

where  $E_{\text{kin},\ell}$  is the kinetic energy of the spherical harmonic degree  $\ell$ , that is calculated from the decomposition of the radial velocity field at the surface into spherical harmonics. Figure 4 shows  $P_{\text{kin}}$  as a function of  $\ell$  for selected simulations. For the simulations with lower rotation rates and large-scale dynamos, the convective power is slightly shifted towards lower  $\ell$ , with peaks between 16 and 20 for set A, 12 and 15 for set B, and 7 and 15 for set C. In simulations with no dynamo, the peak is at considerably larger scales at  $\ell = 4$ . This demonstrates the suppression of large-scale convective flows by magnetic fields. This is reminiscent to results from recent solar-like simulations that suggest that suppression of large-scale convection may be important to maintain a solar-like rotation profile in the Sun (e.g. Hotta et al. 2022; Käpylä 2023). Furthermore, the large-scale convective amplitudes are also in general higher in cases with slower rotation in accordance with linear theory (Chandrasekhar 1961) and various earlier simulations (Featherstone & Hindman 2016; Viviani et al. 2018; Navarrete et al. 2022).

The kinetic helicity, defined as  $\mathcal{H} = \bar{\omega} \cdot \bar{\mathbf{u}}$  is an important component in the operation of the dynamo. It is a proxy of the  $\alpha$ -effect, which is responsible for producing poloidal fields from toroidal fields (and vice versa) by rising or descending and twisting convective eddies (Parker 1955; Steenbeck et al. 1966). In all of our simulations the kinetic helicity is negative (positive) in the northern (southern) hemisphere, as is shown Fig. 3 for run A1. This, combined with a solar-like differential rotation, suggests that an  $\alpha\Omega$  dynamo is operating, in which case the direction of propagation of the dynamo waves is poleward (Parker 1955; Yoshimura 1975). This is consistent with our findings, which will be discussed in more detail in Sect. 3.2.

### 3.1.3. Convective energy transport

The luminosities corresponding to radiative, enthalpy, kinetic energy, cooling and heating fluxes according to Eqs.(31) to (36) of Käpylä (2021) are shown in Fig. 5 for run C4. The enthalpy and

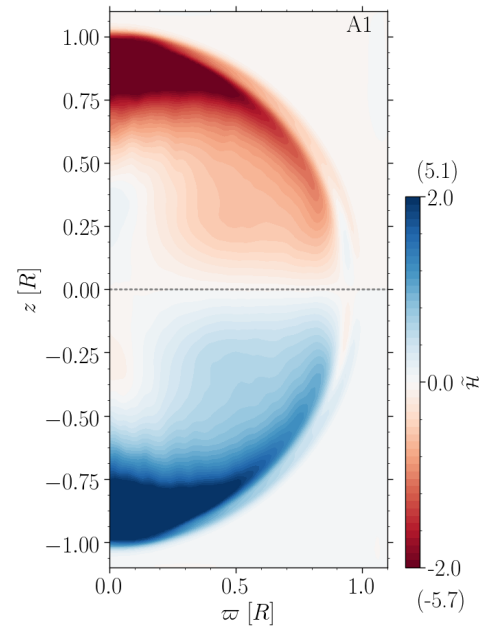


Fig. 3: Azimuthally averaged normalized kinetic helicity,  $\bar{\mathcal{H}} = \mathcal{H}(\varpi, z)/u_{\text{rms}}\omega_{\text{rms}}$ , for simulation A1 with  $\text{Co} = 9.2$  and  $\text{Pr}_{\text{M}} = 0.2$ .

kinetic energy fluxes dominate almost everywhere, except near the surface where the cooling becomes important. This is similar to the results of Brown et al. (2020) and of the rotating runs of Käpylä (2021). The total flux reaches somewhat less than 90 per cent of the luminosity from the heating near the surface. A possible reason for this discrepancy is a non-negligible contribution from the SGS flux.

Sim	$\Delta_{\Omega}^{(r)}$	$\Delta_{\Omega}^{(\theta)}(60^\circ)$	$\Delta_{\Omega}^{(\theta)}(75^\circ)$	$\bar{U}_{\text{mer}}^{\text{rms}}$
A1	0.13	0.038	0.044	$1.8 \cdot 10^{-3}$
A2	0.13	0.035	0.044	$1.2 \cdot 10^{-3}$
A3	0.13	0.039	0.046	$1.9 \cdot 10^{-3}$
A4	0.15	0.044	0.054	$1.9 \cdot 10^{-3}$
A5	0.17	0.052	0.063	$2.0 \cdot 10^{-3}$
A6	0.12	0.037	0.049	$1.2 \cdot 10^{-3}$
A7	0.14	0.041	0.052	$1.9 \cdot 10^{-3}$
A8*	0.28	0.100	0.100	$2.5 \cdot 10^{-3}$
A9	0.18	0.060	0.069	$2.0 \cdot 10^{-3}$
A10	0.14	0.036	0.048	$1.9 \cdot 10^{-3}$
A11	0.12	0.036	0.046	$1.9 \cdot 10^{-3}$
A12*	0.23	0.092	0.091	$2.4 \cdot 10^{-3}$
A13	0.11	0.037	0.046	$1.2 \cdot 10^{-3}$
A14	0.020	0.018	0.019	$1.3 \cdot 10^{-3}$
A15	0.015	0.023	0.025	$1.3 \cdot 10^{-3}$
A16	-0.006	0.019	0.017	$1.1 \cdot 10^{-3}$
<hr/>				
B1	0.067	-0.006	-0.020	$1.4 \cdot 10^{-3}$
B2	0.165	0.073	0.093	$2.4 \cdot 10^{-3}$
B3	0.100	0.062	0.076	$1.8 \cdot 10^{-3}$
B4	0.036	0.051	0.057	$1.6 \cdot 10^{-3}$
B5	-0.029	0.041	0.043	$1.1 \cdot 10^{-3}$
<hr/>				
C1	0.122	0.104	0.122	$1.8 \cdot 10^{-3}$
C2*	0.087	0.067	0.060	$6.7 \cdot 10^{-4}$
C3	0.008	-0.043	-0.069	$1.4 \cdot 10^{-3}$
C4	0.052	0.095	0.101	$1.7 \cdot 10^{-3}$
C5	-0.013	0.086	0.078	$1.6 \cdot 10^{-3}$
C6	-0.058	0.064	0.063	$2.0 \cdot 10^{-3}$

Table 2: Amplitudes of the temporally and azimuthally averaged angular velocity  $\bar{\Omega}(r, \theta)$ . From left to right: the name of the simulation, the amplitudes of the radial and latitudinal differential rotation at  $60^\circ$  and  $75^\circ$  according to in Eqs. (15) and (16), respectively, and the rms value of the meridional flow speed  $\bar{U}_{\text{mer}}^{\text{rms}} = (GM/R)^{-1/2}(\bar{U}_{\varphi}^2 + \bar{U}_z^2)^{1/2}$ .

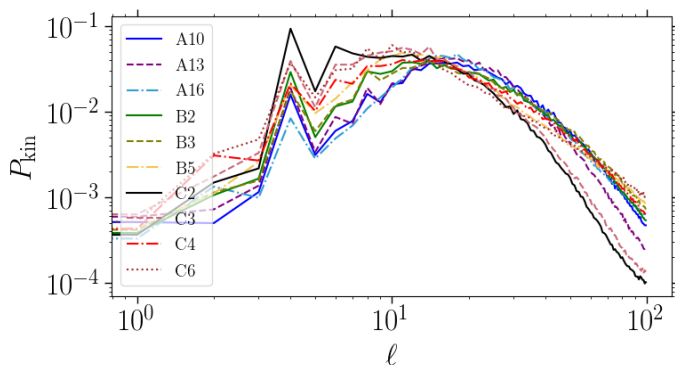


Fig. 4: Normalized convective power as a function of  $\ell$  for simulations A10, A13, A16, B2, B3, B5, C2, C3, C4 and C6.

### 3.2. Dynamo variation

As shown in Table 1, the main differences between the simulations are the input parameters  $\text{Pr}_M$  and the rotation rate. Next, we present the effects of varying these parameters on the large-scale magnetic field.

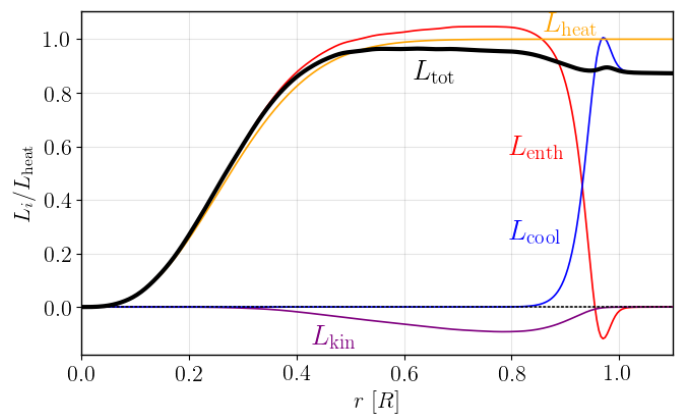


Fig. 5: Luminosity profiles of kinetic energy (purple), cooling (blue), heating (orange) and enthalpy (red) fluxes of run C4.

#### 3.2.1. Dependence on rotation

We have explored simulations with fixed  $\text{Pr}_M$  and varying  $P_{\text{rot}}$  with values between 43 to 90 days. These values were determined using the conversion method outlined in Appendix A of Käpylä (2021). In order to compare the large-scale magnetic field at the three rotation rates used here, we chose runs with comparable magnetic Reynolds numbers and different rotation rates.

Three representative runs with  $\text{Re}_M < 100$  from each set are A6 with  $\text{Re}_M = 75$ , B1 with  $\text{Re}_M = 84$  and C3 with  $\text{Re}_M = 67$ . A6 shows cycles in the azimuthally averaged toroidal magnetic field,  $\bar{B}_\phi(R, \theta, t)$ , as shown in the middle top panel of Figure 6. The cycles were computed using the empirical mode decomposition with the *libeemd* library (Luukko et al. 2016), as in Käpylä (2022). To determine the periods we use  $\bar{B}_\phi(R, \theta, t)$ , from the range  $-60^\circ < \theta < 60^\circ$ . The cycle is determined by taking the mode with the largest energy, and counting the period from the zero crossings of that mode.

Left middle panel of Fig. 6 shows  $\bar{B}_\phi(R, \theta, t)$  for run B1, which also exhibits cycles. The reversals are periodic for most of the run, and it also shows longer term modulation in the northern hemisphere toward the end of the run. The left bottom panel of Fig. 6 is for run C3. Unlike the runs just mentioned, C3 does not exhibit cyclic reversals. However, it does reveal the presence of a dipolar field, with a positive (negative) polarity in the northern (southern) hemisphere. At similar values of magnetic Reynolds number, the third column of Table 1 indicates a slight reduction in  $B_{\text{rms}}$  at lower rotation rates.

Three representative runs with higher magnetic Reynolds number ( $\text{Re}_M \approx 300$ ) and different rotation rates are A15 with  $\text{Re}_M = 300$ , B3 with  $\text{Re}_M = 315$  and C4 with  $\text{Re}_M = 337$ . The right top panel of Fig. 6 shows  $\bar{B}_\phi(R, \theta, t)$  of run A15. This run has irregular reversals with the field mainly distributed from mid-latitudes ( $\pm 45^\circ$ ) to the equator. Near the poles the field is quasi-stationary. The middle center panel of Figure 6 is for B3, where a dipole with a few random reversals is visible with a predominantly negative (positive) polarity at the northern (southern) hemisphere.  $\bar{B}_\phi(R, \theta, t)$  of C4 is shown in the center bottom panel of Fig. 6, where a predominantly positive (negative) polarity. Mollweide projections of the radial magnetic field at the surface of runs A15, B3 and C4 are shown in Fig. 7, where the field is less intense for the runs with lower rotation. In this sense, the  $B_{\text{rms}}$  decreases with decreasing the rotation rate from A15 to B3, while B3 and C4 have similar values. We find that in general

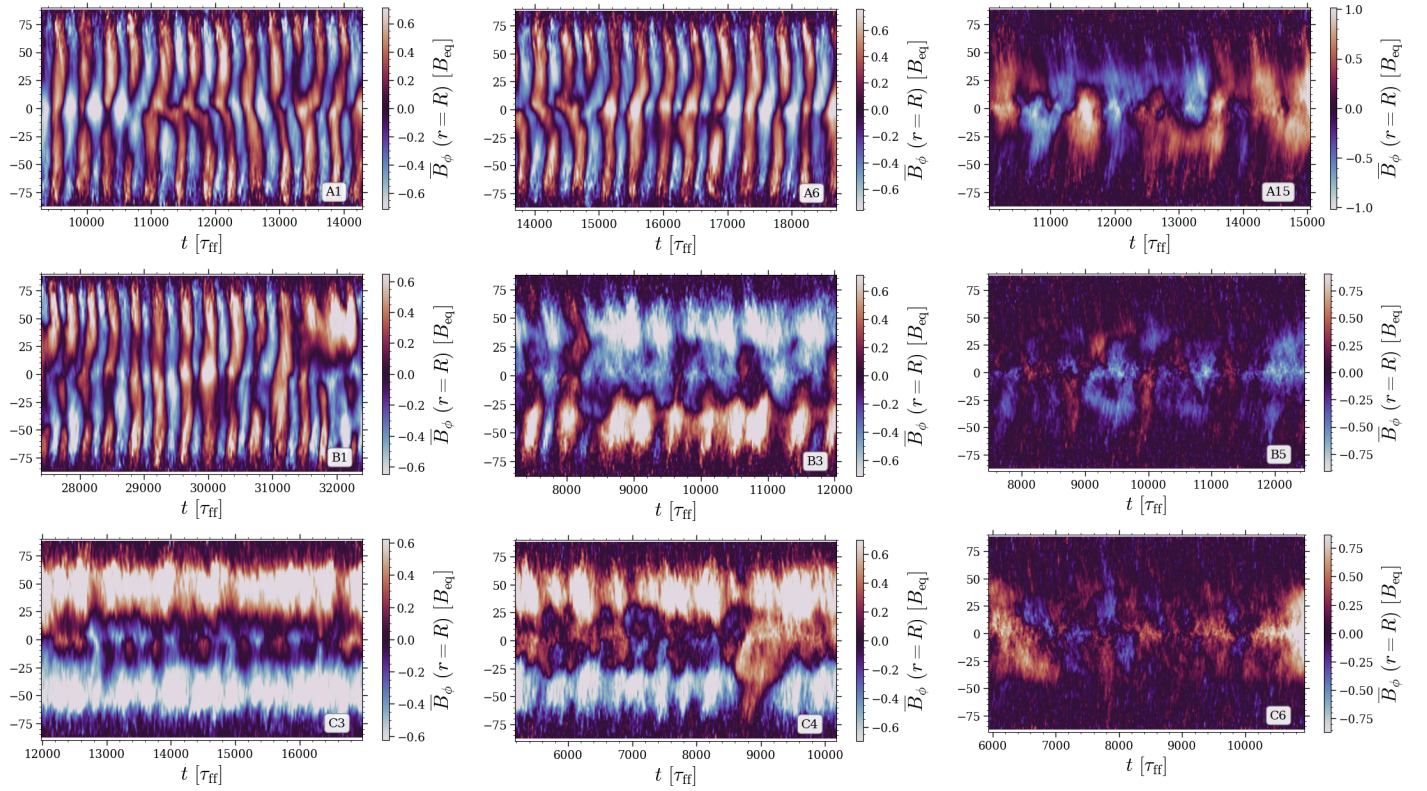


Fig. 6: Azimuthally averaged toroidal magnetic field near the surface of the star as a function of time. The name of the simulation is indicated bottom right of each panel.

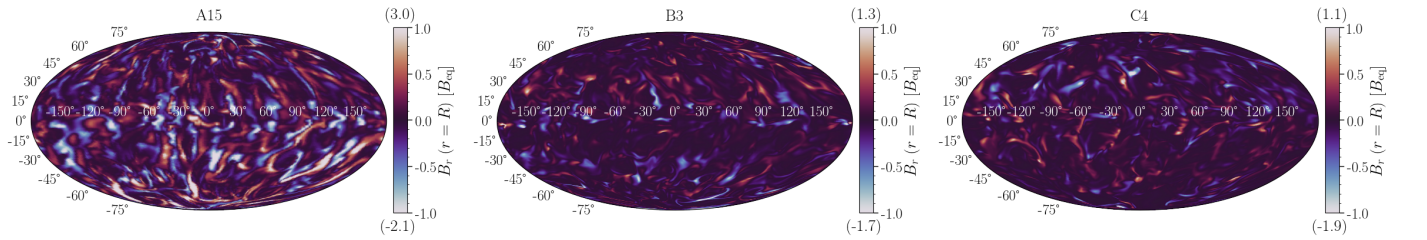


Fig. 7: Mollweide projection of the radial magnetic field  $B_r$  for runs A15, B3 and C4 with  $\text{Re}_M \approx 300$  and different rotation rates.

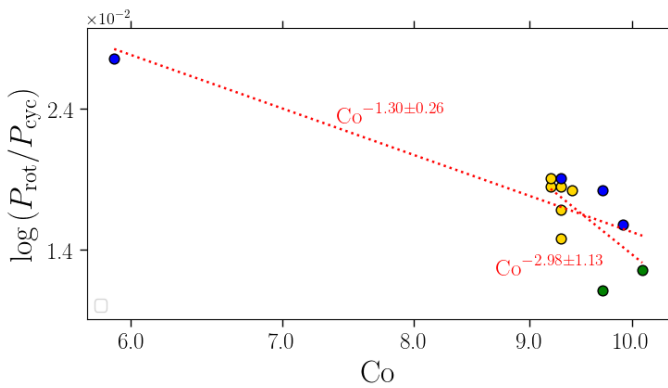


Fig. 8: Rotation period normalized to the cycle period as a function of the global Coriolis number. Green circles are  $\text{Re}_M \sim 100$ , blue for  $70 < \text{Re}_M < 85$ , and yellow is for  $\text{Re}_M \leq 55$ .

the saturation level of the magnetic field increases with  $\text{Re}_M$ . This behavior is likely related to the presence of a small-scale dynamo that produces magnetic fields at spatial scales that are of the same order of magnitude as that of the turbulence. While this was not the focus of our current study this remains an important area for future research.

In Fig. 8 we show the ratio of the rotation period to cycle period as a function of the global Coriolis number. We find that  $P_{\text{rot}}/P_{\text{cyc}} \propto \text{Co}^\beta$  with  $\beta = -1.30 \pm 0.26$ . When considering the data points on the right of the figure, we find that  $\beta = -2.98 \pm 1.13$ . The uncertainty in the slope indicates that we need to take these results with caution. Nevertheless, earlier studies have also found  $\beta < 0$ , for example, [Strugarek et al. \(2017, 2018\)](#); [Warnecke \(2018\)](#); [Viviani et al. \(2018\)](#) with global simulations of solar-like stars. Even when the domain of those simulations differs from the one presented here, the similarity in the relationship between the cycle period and the Coriolis number implies a likeness in the dynamo processes of solar-like and fully convective stars. Nevertheless, the negative slope found here differs from the positive slopes for the inactive and active branches

from observations [Brandenburg et al. \(1998, 2017\)](#). However, also some simulations show  $\beta \gtrsim 0$  ([Guerrero et al. 2019](#); [Käpylä 2022](#)), but the cause of such behavior is currently unclear.

### 3.2.2. Dependence on magnetic Reynolds and Prandtl numbers

Magnetic Prandtl numbers from 0.1 to 10 were used in the simulations. For all the current runs, the magnetic field is predominantly axisymmetric. When converted to physical units, the azimuthally averaged toroidal magnetic field reaches strengths ranging from 10 to 16 kG in our models. These values are higher than those of the reported observations which are up to a few kG (e.g. [Kochukhov 2021](#)). Set A has cycles for  $\text{Pr}_M \leq 2$  with periods ranging from 309 to 471 freefall times, which correspond to 6.3 to 9.6 years, when considering the same time conversion factor used by [Käpylä \(2021\)](#). Run B1 also shows cycles with a period of 274 freefall times. Table 3 lists the values of  $\nu$ ,  $\eta$ , the cycle periods (if applicable) together with the corresponding standard deviation for all the simulations presented here. We found that the calculated length of the cycle periods of the runs of set A has a very slight increase when increasing the magnetic Reynolds number as  $P_{\text{cyc}} \propto \text{Re}_M^\alpha$  with  $\alpha = 0.25 \pm 0.14$ . Additionally, when considering the runs with similar  $\text{Re}_M$  and different  $\text{Pr}_M$ , we found that the cycle period is virtually independent of  $\text{Pr}_M$  in the parameter regime explored here.

The azimuthally averaged toroidal magnetic field  $\bar{B}_\phi(R, \theta, t)$  is shown in Figure 6 for a set of representative runs. The top panels are for three runs of set A, which have the same rotation period and increasing  $\text{Re}_M$  from left to right. The top left panel is for run A1 with  $\text{Re}_M = 55$ , with  $P_{\text{cyc}} = 320 \pm 10$  freefall times. The top center panel is for run A6 with  $\text{Re}_M = 75$  and  $P_{\text{cyc}} = 326 \pm 11$  freefall times. In these cases the field is distributed in latitudes  $|\theta| \lesssim 80^\circ$ . Simulations with higher values of  $\text{Pr}_M$  and  $\text{Re}_M$ , such as run A15 with  $\text{Re}_M = 300$ , result in the loss of cycles and the emergence of irregular solutions. Similar irregularity of dynamo solutions has previously been observed in simulations with high  $\text{Re}_M$  (e.g. [Käpylä et al. 2017](#)), but the exact mechanisms is still unknown. In this case, the field is distributed at latitudes  $|\theta| \lesssim 50$  and also exhibits quasi-stationary solutions near the poles.

The polarity of the field changes from the surface to  $r = 0.5R$ . Figure 9 shows  $\bar{B}_\phi$  at  $r = 0.5R$  for runs A1 and A15. In simulations with cycles, such as A1, the cycles are visible throughout the convection zone. However, for runs with higher magnetic Prandtl number ( $\text{Pr}_M > 2$ ), such as A15 the azimuthally averaged toroidal magnetic field changes with depth and shows less clear magnetic structures in the deeper layers.

The second row of Fig. 6 shows three runs from set B which have the same rotation rate and increasing  $\text{Re}_M$ . The left panel is for run B1 with  $\text{Re}_M = 84$ , which exhibits a cycle with  $P_{\text{cyc}} = 274 \pm 38$  freefall times, as well as longer reversals or disappearing cycles toward the end of the run. In this run the field is distributed at latitudes  $|\theta| \lesssim 80^\circ$ . The center panel is for run B3 with  $\text{Re}_M = 315$ , which exhibits an irregular solution with few polarity reversals and predominantly quasi-static fields. In this case, the field spans slightly less latitudinally, distributed at latitudes  $|\theta| \lesssim 75^\circ$ . The right center panel Fig. 6 shows run B5, which has the highest  $\text{Pr}_M$  and  $\text{Re}_M$  in this set with  $\text{Pr}_M = 10$  and  $\text{Re}_M = 1360$ . The field is more concentrated toward the equator (at latitudes  $|\theta| \lesssim 50^\circ$ ) with seemingly irregular reversals. Similar to run A15, B5 also has a quasi-stationary solution near the poles. The third row of Fig. 6 are for runs of set C, which have the

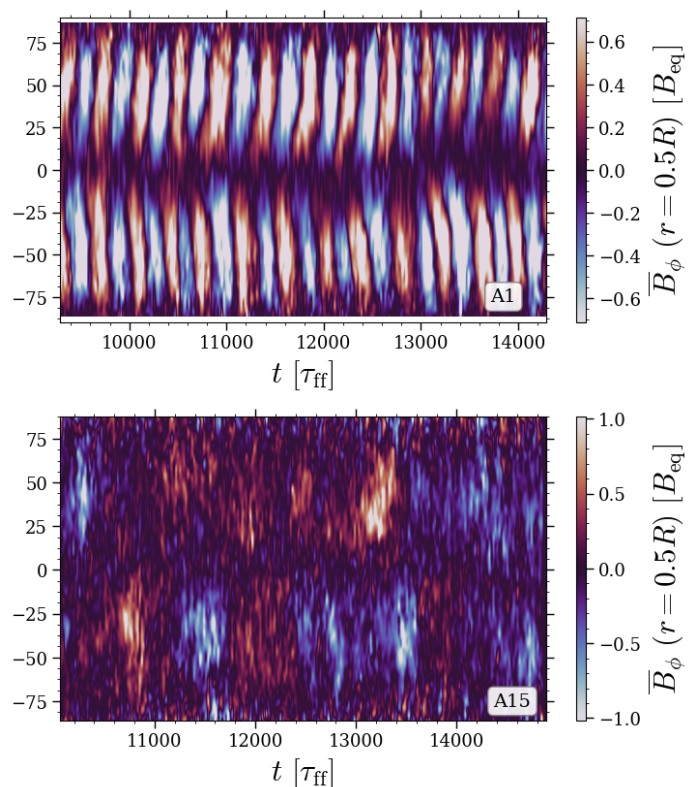


Fig. 9: Azimuthally averaged toroidal magnetic field at  $r = 0.5$  for simulations A1 (top) and A15 (bottom) with  $\text{Re}_M = 55$  and  $\text{Re}_M = 300$ , respectively.

slowest rotation in the present work, with increasing  $\text{Re}_M$  from left to right. Runs C3 with  $\text{Re}_M = 67$  and C4 with  $\text{Re}_M = 337$  show a predominantly quasi-static dipolar field, which spans latitudes  $|\theta| \lesssim 75^\circ$ . A similar dipolar field was reported by [Moutou et al. \(2017\)](#) for the fully convective and slow-rotating M dwarf GJ 1289. However, in our models the toroidal magnetic energy is dominant (see Table 3), whereas the large-scale magnetic field of GJ 1289 is purely poloidal. Run C6 with  $\text{Re}_M = 1419$  has a field concentrated near the equator and the large-scale structures are less clear than in C3 and C4.

The radial magnetic field,  $B_r$ , also varies as a function of  $\text{Re}_M$ . Mollweide projections of the radial magnetic field for runs B1, B2 and B5, with increasing  $\text{Re}_M$  from left to right are presented in Figure 10. The main differences here are the structure and maximum values of the magnetic field strength. The size of the structures in runs B1 and B2 are similar, but the strength of the field is slightly higher in B2. Run B5 has smaller field structures than in the previous cases, and the magnetic field strength is higher.

Table 3 lists the energy densities of the simulations. The total magnetic energy  $E_{\text{mag}}$  is a significant fraction of the kinetic energy density in all of the runs with dynamos, sometimes also exceeding it. One may expect that  $E_{\text{mag}}$  grows with increasing  $\text{Re}_M$  ( $\text{Pr}_M$ ), as found in other works (e.g., [Käpylä et al. 2017](#)). In this regard, there is no discernible trend in the simulations shown here in terms of the variation of  $E_{\text{mag}}$ . Since the kinetic energy density,  $E_{\text{kin}}$ , decreases with increasing  $\text{Pr}_M$  the ratio  $E_{\text{mag}}/E_{\text{kin}}$  grows. The decrease of the kinetic energy can be explained because at large  $\text{Pr}_M$ , it is converted into magnetic energy more efficiently.



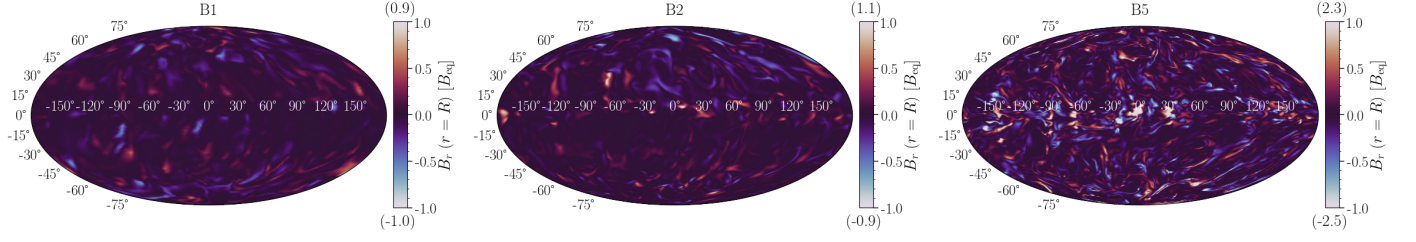


Fig. 10: Mollweide projection of the radial magnetic field  $B_r$  for runs with the same rotation rate and different  $\text{Re}_M$ , B1 with  $\text{Re}_M = 84$ , B2 with  $\text{Re}_M = 168$ , and B5 with  $\text{Re}_M = 1360$ .

Sim	$\nu$	$\eta$	Cycles	$\sigma$	$\tilde{E}_{\text{mag}}$	$E_{\text{mag}}^{\text{tor}}/E_{\text{mag}}$	$E_{\text{mag}}^{\text{pol}}/E_{\text{mag}}$	$\tilde{E}_{\text{kin}}^{\text{DR}}$	$\tilde{E}_{\text{kin}}^{\text{MC}}$
A1	$1.0 \cdot 10^{-5}$	$1.0 \cdot 10^{-4}$	320	10	0.86	0.23	0.07	0.23	0.01
A2	$6.9 \cdot 10^{-6}$	$6.9 \cdot 10^{-5}$	309	7	0.89	0.20	0.06	0.27	0.02
A3	$2.0 \cdot 10^{-5}$	$1.0 \cdot 10^{-4}$	350	13	0.85	0.24	0.06	0.24	0.06
A4	$5.0 \cdot 10^{-5}$	$1.0 \cdot 10^{-4}$	320	33	0.64	0.20	0.06	0.31	0.02
A5	$7.0 \cdot 10^{-5}$	$1.0 \cdot 10^{-4}$	310	72	0.41	0.24	0.06	0.34	0.02
A6	$4.9 \cdot 10^{-5}$	$6.9 \cdot 10^{-5}$	326	11	0.84	0.21	0.05	0.31	0.02
A7	$5.0 \cdot 10^{-5}$	$1.0 \cdot 10^{-4}$	324	17	0.68	0.25	0.06	0.31	0.02
A8*	$7.0 \cdot 10^{-5}$	$3.5 \cdot 10^{-4}$	-	-	-	-	-	0.55	0.01
A9	$7.0 \cdot 10^{-5}$	$1.4 \cdot 10^{-4}$	387	63	0.39	0.28	0.07	0.32	0.02
A10	$5.0 \cdot 10^{-5}$	$5.0 \cdot 10^{-5}$	471	84	0.77	0.16	0.04	0.32	0.02
A11	$7.0 \cdot 10^{-5}$	$7.0 \cdot 10^{-5}$	368	23	0.78	0.20	0.05	0.30	0.02
A12*	$1.0 \cdot 10^{-4}$	$1.0 \cdot 10^{-4}$	-	-	-	-	-	0.54	0.02
A13	$1.0 \cdot 10^{-4}$	$5.0 \cdot 10^{-5}$	437	13	1.44	0.15	0.04	0.32	0.02
A14	$1.0 \cdot 10^{-4}$	$2.0 \cdot 10^{-5}$	-	-	1.68	0.08	0.03	0.16	0.02
A15	$1.0 \cdot 10^{-4}$	$7.1 \cdot 10^{-5}$	-	-	1.46	0.06	0.02	0.14	0.02
A16	$1.0 \cdot 10^{-4}$	$1.0 \cdot 10^{-5}$	-	-	1.74	0.03	0.02	0.10	0.01
B1	$3.6 \cdot 10^{-5}$	$7.2 \cdot 10^{-5}$	274	38	0.45	0.20	0.04	0.33	0.02
B2	$3.6 \cdot 10^{-5}$	$3.6 \cdot 10^{-5}$	-	-	0.53	0.16	0.03	0.38	0.02
B3	$3.6 \cdot 10^{-5}$	$1.8 \cdot 10^{-5}$	-	-	0.80	0.11	0.03	0.30	0.02
B4	$3.6 \cdot 10^{-5}$	$7.2 \cdot 10^{-6}$	-	-	1.21	0.06	0.02	0.22	0.02
B5	$3.6 \cdot 10^{-5}$	$3.6 \cdot 10^{-6}$	-	-	1.13	0.03	0.02	0.014	0.01
C1	$2.5 \cdot 10^{-5}$	$2.5 \cdot 10^{-5}$	-	-	0.67	0.17	0.03	0.31	0.03
C2*	$1.0 \cdot 10^{-4}$	$2.0 \cdot 10^{-4}$	-	-	-	-	-	0.14	0.12
C3	$1.0 \cdot 10^{-4}$	$1.0 \cdot 10^{-4}$	-	-	0.28	0.34	0.03	0.44	0.02
C4	$3.6 \cdot 10^{-5}$	$1.8 \cdot 10^{-5}$	-	-	0.81	0.12	0.03	0.25	0.03
C5	$3.6 \cdot 10^{-5}$	$7.2 \cdot 10^{-6}$	-	-	1.72	0.10	0.03	0.19	0.03
C6	$3.6 \cdot 10^{-5}$	$3.6 \cdot 10^{-6}$	-	-	1.06	0.04	0.02	0.16	0.02

Table 3: Columns from left to right indicate normalized kinematic viscosity  $\tilde{\nu} = (RGM)^{-1/2}\nu$ , normalized magnetic diffusivity  $\tilde{\eta} = (RGM)^{-1/2}\eta$ , cycle periods, and their standard deviations, both in terms of  $t_{\text{ff}}$ , and energy densities if applicable. The magnetic energy density is  $E_{\text{mag}} = \langle \mathbf{B}^2 / 2\mu_0 \rangle$ , where the brackets indicate volume and time average within the radius of the star. The kinetic energy density is  $E_{\text{kin}} = \frac{1}{2} \langle \rho \mathbf{U}^2 \rangle$ . The energy density for the azimuthally averaged toroidal and poloidal fields are given by  $E_{\text{mag}}^{\text{tor}} = \langle \overline{\mathbf{B}}_{\phi}^2 / 2\mu_0 \rangle$ , and  $E_{\text{mag}}^{\text{pol}} = (\langle \overline{\mathbf{B}}_{\varpi}^2 + \overline{\mathbf{B}}_z^2 \rangle) / 2\mu_0$ , respectively. The energy density for the differential rotation and meridional circulation are given by  $E_{\text{kin}}^{\text{DR}} = \frac{1}{2} \langle \rho \overline{\mathbf{U}}_{\phi}^2 \rangle$ , and  $E_{\text{kin}}^{\text{MC}} = \frac{1}{2} \langle \rho (\overline{\mathbf{U}}_{\varpi}^2 + \overline{\mathbf{U}}_z^2) \rangle$ , respectively. Tildes over energies refer to normalization by  $E_{\text{kin}}$ . Asterisks indicate runs with no dynamo.

At low  $\text{Pr}_M$  the kinematic, exponentially growing, regime lasts longer than in the simulations with high  $\text{Pr}_M$ . Figure 11 shows the evolution of  $E_{\text{mag}}$  and  $E_{\text{kin}}$  in the kinematic and saturated regimes for runs A4 and A16. The kinematic regime of simulation A4 lasted about 10 times longer than the kinematic regime of run A16. It can be seen that in simulation A4,  $E_{\text{mag}}$  is amplified by six orders of magnitude. In the saturated regime, both energies are comparable such that  $E_{\text{kin}}$  is about 1.5 times  $E_{\text{mag}}$ . However, in simulation A16 the kinetic energy density is slightly reduced, while the magnetic energy density is increased by a factor of roughly 1.8. The  $\text{Pr}_M$  at which  $E_{\text{mag}}$  overcomes

$E_{\text{kin}}$  occurs at  $\text{Pr}_M > 1$  for sets A and B, and at  $\text{Pr}_M > 2$  for set C. A similar behaviour of the kinetic and magnetic energy densities was reported before by Browning (2008) for simulations of fully convective stars. In run Cm2 of that work with  $\text{Pr}_M = 5$ ,  $E_{\text{mag}}/E_{\text{kin}} \leq 1$ , while Cm with  $\text{Pr}_M = 8$  has  $E_{\text{mag}}/E_{\text{kin}} = 1.2$ .

Table 3 also includes the energy densities of mean toroidal ( $E_{\text{mag}}^{\text{tor}}$ ) and poloidal ( $E_{\text{mag}}^{\text{pol}}$ ) magnetic fields (see columns 8 and 9).  $E_{\text{mag}}^{\text{tor}}$  accounts for up to 30% of total magnetic energy density and, in general, diminishes as  $\text{Re}_M$  increases.  $E_{\text{mag}}^{\text{pol}}$  is less than 10% of  $E_{\text{mag}}$  for almost all simulations. In general, the

ratio of the energy of the mean field to total energy decreases for high magnetic Reynolds numbers. Figure 12 shows the saturation level of the mean field as a function of  $Re_M$  for subsets of simulations from sets A and B. We do not find a clear trend in the saturation level of the mean energy as a function of the magnetic Reynolds number. A decrease in the mean energy with the inverse magnetic Reynolds number is usually associated with catastrophic quenching (e.g. Cattaneo & Vainshtein 1991; Brandenburg 2001). It can be interpreted as an outcome of magnetic helicity conservation, which becomes important as  $Re_M$  grows (e.g. Brandenburg & Subramanian 2005). Nevertheless, the boundary conditions in our simulations do allow magnetic helicity fluxes.

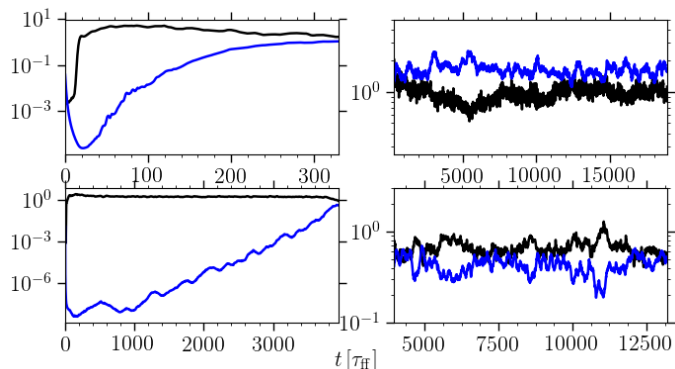


Fig. 11: Time evolution of the kinetic (black) and magnetic (blue) energy densities in the kinematic (left) and saturated (right) regimes for simulations A16 with  $Pr_M = 10$  (top) and A4  $Pr_M = 0.5$  (bottom). The energies are normalized by  $E_{kin}$ .

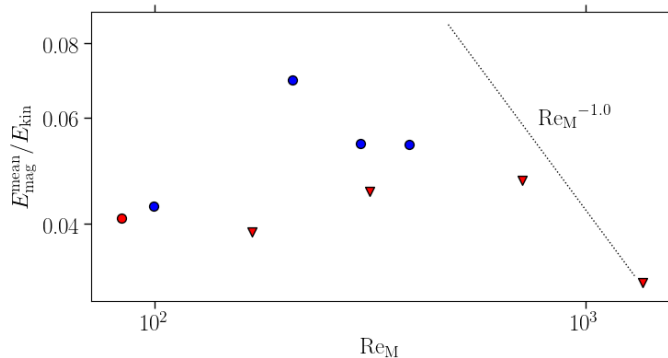


Fig. 12: Mean magnetic energy normalized by kinetic energy as a function of the magnetic Reynolds number. The blue markers are for the last four simulations of set A; the red markers are for the simulations of set B. Circles (triangles) are for runs with  $200^3$  ( $576^3$ ) of resolution. The dotted line corresponds to a power law that shows how a decrease in mean energy with the inverse magnetic Reynolds number might look like.

Furthermore, the kinetic energy density of the differential rotation,  $E_{kin}^{DR}$ , and meridional circulation,  $E_{kin}^{MC}$ , are given in Table 3. For simulations with a dynamo  $E_{kin}^{DR}$  decreases at higher  $Re_M$ , while for simulations A8 and A12 with no dynamo  $E_{kin}^{DR}$  is significantly higher. More specifically the runs without a dynamo in set A exhibit roughly five times higher  $E_{kin}^{DR}$  than runs with a dynamo in the same set. This indicates magnetic quenching of differential rotation. In all of the simulations discussed here,

$E_{kin}^{MC}$  is around 1-3 per cent of  $E_{kin}$ , with the exception of C2, where  $E_{kin}^{MC} \approx 0.12E_{kin}$ .

#### 4. Summary and conclusions

We have performed a large sample of simulations of fully convective M dwarfs using the star-in-a-box setup presented in Käpylä (2021). We used the stellar parameters for an M5 dwarf with  $0.21M_{\odot}$  at three rotation rates corresponding to  $P_{rot} = 43, 61$  and  $90$  days, and varied the magnetic Prandtl number from 0.1 to 10. Our simulations explore the intermediate to slowly rotating regime. Consistent with previous work by Käpylä (2021), we find solar-like differential rotation in the simulations presented here.

We found different solutions for the large-scale magnetic field depending on the rotation period and the magnetic Prandtl number, which, in our models, fixes the magnetic Reynolds number. For the simulations with  $\tilde{\Omega} = 1.0$  (set A) and  $Re_M \leq 105$ , the large-scale magnetic field is cyclic, with  $P_{cyc}$  ranging from 309 to 471 freefall times. In this set, we found a slight increase in the length of the cycle period with increasing  $Re_M$ . For larger  $Re_M$ , no clear cycles are found and instead the behaviour of the magnetic field and its reversals become irregular. For the simulations with  $\tilde{\Omega} = 0.7$  (set B) we found cycles for run B1 with  $Re_M = 84$ , while for higher values of  $Re_M$  the reversals are less regular, and instead, a quasi-static configuration is found. For the highest  $Re_M$ , the solutions become irregular. For the case with the lowest rotation rate ( $\tilde{\Omega} = 0.5$ ), the field is mainly dipolar for  $Re_M \leq 750$ . At higher magnetic Reynolds numbers the magnetic field is predominantly irregular and concentrated at mid-latitudes, with quasi-stationary fields near the poles. We note that in the three sets, the large-scale field is irregular and concentrated near the equator for the highest  $Pr_M$  ( $Re_M$ ). Additionally, the rms-velocity increases for decreasing rotation for comparable  $Re_M$ . We also note that for a few of the simulations, particularly A8, A12 and C2, no dynamo was found, because  $Re_M$  was below the critical value to drive a large-scale dynamo.

Furthermore, the ratio  $P_{rot}/P_{cyc}$  decreases with the Coriolis number, similar to the simulations of solar-like stars by Strugarek et al. (2017, 2018); Warnecke (2018); Viviani et al. (2018). Our results confirm the important role of rotation and dimensionless parameters such as  $Re_M$  and the  $Pr_M$  in determining the properties of fully convective dynamos. Depending on the parameters, the magnetic field can show a clear cyclic behaviour with the cycle period influenced by the rotation rate and dimensionless parameters such as  $Re_M$  ( $Pr_M$ ). The large-scale magnetic field shows cycles for low and modest values of  $Re_M$  but the cycles are lost for highest magnetic Reynolds numbers where irregular or quasi-static fields dominate. A similar loss of cyclic solutions was reported by Käpylä et al. (2017) who also increased  $Pr_M$  to increase  $Re_M$ . Whether the behavior of the dynamo changes if  $Re_M$  is fixed and  $Pr_M$  is lowered is yet an open question. This is also closer to the parameter regime of late-type stars where  $Pr_M \ll 1$  and  $Re_M \gg 1$ , but such parameter regime is extremely challenging numerically.

A very tentative comparison can be pursued with the Proxima Centauri system, where Klein et al. (2021) inferred a seven-year activity cycle. In principle the activity cycle inferred in our simulations is in the range from five to nine years, and thus consistent with the observed data. We note that this comparison is preliminary and even though the rotation rate we adopt here is similar, the magnetic Prandtl number is likely to be different, and even larger differences concern the magnetic Reynolds number in the star in comparison to the simulation. As it is well known

that the solutions for the magnetic field depend on these parameters, leading to uncertainty in the possible interpretation. It is nevertheless encouraging that the behaviour found in the simulations is relatively similar.

Overall, the study presented here consists of, to our knowledge, the largest exploration of the parameter space for dynamo models of fully convective M dwarfs. Uncertainties remain for instance regarding the role of the magnetic Reynolds number, which will still be much larger in realistic systems. While a clear signature of a small-scale dynamo (SSD) is not found in our simulations, the expectation is that SSD are present at larger magnetic Reynolds numbers and interact with the large-scale dynamo, thereby changing the solution.

*Acknowledgements.* CAOR, DRGS and JPH thank for funding via Fondecyt Regular (project code 1201280). CAOR, DRGS and R.E.M. gratefully acknowledge support by the ANID BASAL projects ACE210002 and FB210003. DRGS and R.E.M. gratefully acknowledge support by the FONDECYT Regular 1190621. DRGS thanks for funding via the Alexander von Humboldt - Foundation, Bonn, Germany. PJK acknowledges financial support from DFG Heisenberg programme grant No. KA 4825/4-1. FHN acknowledges financial support by the DAAD (Deutscher Akademischer Austauschdienst; code 91723643). The simulations were made using the Kultrun cluster hosted at the Departamento de Astronomía, Universidad de Concepción, and on HLRN-IV under project grant hhp00052.

## References

- Augustson, K. C., Brun, A. S., & Toomre, J. 2019, *ApJ*, 876, 83
- Bice, C. P. & Toomre, J. 2020, *ApJ*, 893, 107
- Brandenburg, A. 2001, *ApJ*, 550, 824
- Brandenburg, A., Mathur, S., & Metcalfe, T. S. 2017, *ApJ*, 845, 79
- Brandenburg, A., Saar, S. H., & Turpin, C. R. 1998, *ApJ*, 498, L51
- Brandenburg, A. & Subramanian, K. 2005, *Phys. Rep.*, 417, 1
- Brown, B. P., Oishi, J. S., Vasil, G. M., Lecoanet, D., & Burns, K. J. 2020, *ApJ*, 902, L3
- Browning, M. K. 2008, *ApJ*, 676, 1262
- Brun, A. S. & Browning, M. K. 2017, *Liv. Rev. Sol. Phys.*, 14, 4
- Brun, A. S., Miesch, M. S., & Toomre, J. 2004, *ApJ*, 614, 1073
- Cattaneo, F. & Vainshtein, S. I. 1991, *ApJ*, 376, L21
- Chabrier, G. & Baraffe, I. 1997, *A&A*, 327, 1039
- Chandrasekhar, S. 1961, *Hydrodynamic and hydromagnetic stability*
- Dobler, W., Stix, M., & Brandenburg, A. 2006, *ApJ*, 638, 336
- Featherstone, N. A. & Hindman, B. W. 2016, *ApJ*, 830, L15
- Guerrero, G., Zaire, B., Smolarkiewicz, P. K., et al. 2019, *ApJ*, 880, 6
- Hotta, H., Kusano, K., & Shimada, R. 2022, *ApJ*, 933, 199
- Jermyn, A. S., Anders, E. H., Lecoanet, D., & Cantiello, M. 2022, *ApJS*, 262, 19
- Käpylä. 2021, *A&A*, 651, A66
- Käpylä, P. J. 2022, *ApJ*, 931, L17
- Käpylä, P. J. 2023, *A&A*, 669, A98
- Käpylä, P. J., Gent, F. A., Olsper, N., Käpylä, M. J., & Brandenburg, A. 2020, *Geophys. Astrophys. Fluid Dyn.*, 114, 8
- Käpylä, P. J., Käpylä, M., Olsper, N., Warnecke, J., & Brandenburg, A. 2017, *A&A*, 599, A4
- Käpylä, P. J., Käpylä, M. J., & Brandenburg, A. 2018, *Astron. Nachr.*, 339, 127
- Klein, B., Donati, J.-F., Hébrard, É. M., et al. 2021, *MNRAS*, 500, 1844
- Kochukhov, O. 2021, *Astron. Astrophys. Rev.*, 29, 1
- Luukko, P. J., Helske, J., & Räsänen, E. 2016, *Comput. Stat.*, 31, 545
- Morin, J., Donati, J.-F., Petit, P., et al. 2010, *MNRAS*, 407, 2269
- Moutou, C., Hébrard, E., Morin, J., et al. 2017, *MNRAS*, 472, 4563
- Navarrete, F. H., Schleicher, D. R., Käpylä, P. J., Ortiz-Rodríguez, C. A., & Banerjee, R. 2022, *A&A*, 667, A164
- Newton, E. R., Irwin, J., Charbonneau, D., et al. 2017, *ApJ*, 834, 85
- Parker, E. N. 1955, *ApJ*, 122, 293
- Pencil Code Collaboration, Brandenburg, A., Johansen, A., et al. 2021, *J. Open Source Softw.*, 6, 2807
- Reiners, A., Shulyak, D., Käpylä, P. J., et al. 2022, *A&A*, 662, A41
- Rogachevskii, I. & Kleeorin, N. 2015, *J. Plasma Phys.*, 81, 395810504
- Saar, S. H. & Linsky, J. L. 1985, *ApJ*, 299, L47
- Schekochihin, A. A., Isakov, A. B., Cowley, S. C., et al. 2007, *New J. Phys.*, 9, 300
- Schrinner, M., Petitdemange, L., & Dormy, E. 2012, *ApJ*, 752, 121
- Steenbeck, M., Krause, F., & Rädler, K.-H. 1966, *Z. Naturf. A*, 21, 369
- Strugarek, A., Beaudoin, P., Charbonneau, P., & Brun, A. 2018, *ApJ*, 863, 35
- Strugarek, A., Beaudoin, P., Charbonneau, P., Brun, A., & do Nascimento Jr, J.-D. 2017, *Science*, 357, 185
- Viviani, M., Warnecke, J., Käpylä, M. J., et al. 2018, *A&A*, 616, A160
- Warnecke, J. 2018, *A&A*, 616, A72
- Wright, N. J. & Drake, J. J. 2016, *Nature*, 535, 526
- Wright, N. J., Newton, E. R., Williams, P. K., Drake, J. J., & Yadav, R. K. 2018, *MNRAS*, 479, 2351
- Yadav, R. K., Christensen, U. R., Morin, J., et al. 2015, *ApJ*, 813, L31
- Yadav, R. K., Christensen, U. R., Wolk, S. J., & Poppenhaeger, K. 2016, *ApJ*, 833, L28
- Yoshimura, H. 1975, *ApJ*, 201, 740